Project Number 282910

ÉCLAIRE

Effects of Climate Change on Air Pollution Impacts and Response Strategies for European Ecosystems

Seventh Framework Programme

Theme: Environment

D5.2 Range of future evolution of global, hemispheric and European ozone

Due date of deliverable: **30/09/2014** Actual submission date: **11/2/2015**

Start Date of Project: **01/10/2011** Duration: **36 months**

Organisation name of lead contractor for this deliverable : JRC

Project co-funded by the European Commission within the Seventh Framework Programme		
Dissemination Level		
PU	Public	x
PP	Restricted to other programme participants (including the Commission Services)	☐
RE	Restricted to a group specified by the consortium (including the Commission Services)	☐
CO	Confidential, only for members of the consortium (including the Commission Services)	☐

1. Executive Summary

An updated version of the LMDz-INCA model has been used to evaluate a range of RCP emission scenarios, as well as new air pollution emission inventories developed in the frame of the ECLAIRE/ECLIPSE/PEGASOS projects.

A detailed description of ammonium sulfate-nitrate and coarse-aerosol nitrate formation was included in LMDz-INCA model. Good agreement of surface aerosol concentrations and aerosol optical depth was found for Europe and North America. Nitrogen and sulfur deposition were in reasonable agreement in Europe and North America, but systemically underestimated in Eastern Asia.
Model calculations suggest under the RCP scenarios SO4 burden is strongly declining, while nitrate and ammonium aerosol burdens are more constant. Agricultural emission of NH3 may therefore maintain higher levels of cooling than assumed in previous studies. The fraction of ammonium in nitrogen deposition is increasing from about 60-80 % in China. These results are driven by increasing agricultural ammonia emissions in the RCP emission scenario, subject to high uncertainty.

Comparison of the summer ozone distributions between 2050 and 2010 using the ECLIPSE5.0 emission scenario indicates ozone decreases by up to 7 ppbv in Northern America and by 4-5 ppb in Europe. In China, SE Asia, and India, ozone increases by up to 7 ppb due to increased anthropogenic emissions in these regions. Climate and land use change by 2050 may augment isoprene emission and lead to ozone increases in large portions of the Northern Hemisphere up to 4,5 ppb, potentially off-setting the ozone reductions by anthropogenic emissions in Europe and North America. However, when including the effect of increasing CO2 on reducing the isoprene emissions, the effect on ozone is much less, with two current parameterizations strongly disagreeing.

Controlling methane and air pollution emissions in Asia is going to be of critical importance for ozone air quality in Europe.

Objectives

Selected scenarios of future emissions provided by IPCC AR5 RCPs, and possibly other scenarios, will be used to evaluate the possible global, hemispheric and European evolution of ozone and other air pollutants for 2030, 2050 and 2100. LMDz-INCA- ORCHIDEE will be used to simulate the future impact of biogenic and soil emissions of ozone and aerosol precursors on future levels of pollutants, especially O_3 and reactive N-compounds. The uncertainty of these emissions will be estimated using emission datasets developed in WP2.2, accounting for future climate and changes in land use a well as anthropogenic and biogenic emissions. Sensitivity simulations will be carried out in order to discriminate the relative contributions of the various changes on the level of pollutants in Europe and interactions with pollution on global scale (TM5, LMDz and, up to 2050, EMEP).

D5.2 reports on the range of future evolutions of global, hemispheric and European O_3, O_3 precursors, and aerosol using a range of anthropogenic and natural emissions (*Month 36*)

2. Activities

CNRS made major upgrades to their model and performed extensive simulations of a variety of RCP scenarios.

JRC performed TM5 FASST analysis of emission scenarios, and –through the CLRTAP Task Force Hemispheric Transport of Air Pollution (TF HTAP) organized and analysed future air pollution scenarios.

3. Results from CNRS LMDz-INCA model calculations

3.1. The LMDz-INCA model standard version

CNRS used the LMDz-INCA global chemistry-aerosol-climate model coupling on-line the LMDz (Laboratoire de Météorologie Dynamique, version 5) General Circulation Model (Hourdin et al., 2006) and the INCA (INteraction with Chemistry and Aerosols, version 4) model (Hauglustaine et al., 2004). The interaction between the atmosphere and the land surface is ensured through the coupling of LMDz with the ORCHIDEE (ORganizing Carbon and Hydrology In Dynamic Ecosystems, version 9) dynamical vegetation model (Krinner et al., 2005). In the present configuration, the model includes 39 hybrid vertical levels extending up to 80 km. The horizontal resolution is 1.9° in latitude and 3.75° in longitude. The primitive equations in the GCM are solved with a 3 min time-step, large-scale transport of tracers is carried out every 15 min, and physical and chemical processes are calculated at a 30 min time interval. For a more detailed description and an extended evaluation of the GCM we refer to Hourdin et al. (2006). The large-scale advection of tracers is calculated based on a monotonic finite-volume second-order scheme (Van Leer, 1977; Hourdin and Armengaud 1999). Deep convection is parameterized according to the scheme of Emanuel (1991). The turbulent mixing in the planetary boundary layer is based on a local second-order closure formalism (Louis, 1989). The transport and mixing of tracers in the LMDz GCM have been investigated and evaluated against observations for both inert tracers and radioactive tracers (e.g., Hourdin and Issartel, 2000; Hauglustaine et al., 2004; Rivier et al., 2005) and in the framework of inverse modelling studies (e.g., Bousquet et al., 2005; Pison et al., 2009; Bousquet et al., 2010).

INCA includes a state-of-the-art CH_4-NOx-CO-NMHC-O_3 tropospheric photochemistry (Hauglustaine et al., 2004; Folberth et al., 2006). The tropospheric photochemistry and aerosols scheme used in this model version is described through a total of 123 tracers including 22 tracers to represent aerosols. The model includes 234 homogeneous chemical reactions, 43 photolytic reactions and 30 heterogeneous reactions. Please refer to Hauglustaine et al. (2004) and Folberth et al. (2006) for the list of reactions included in the tropospheric chemistry scheme. The gas-phase version of the model has been extensively compared to observations in the lower-troposphere and in the upper-troposphere. For aerosols, the INCA model simulates the distribution of aerosols with anthropogenic sources such as sulfates, nitrates, black carbon, particulate organic matter, as well as natural aerosols such as sea-salt

and dust. The aerosol model keeps track of both the number and the mass of aerosols using a modal approach to treat the size distribution, which is described by a superposition of 5 log-normal modes (Schulz et al., 1998; Schulz, 2007), each with fixed spread. To treat the optically relevant aerosol size diversity, particle modes exist for three ranges: sub-micronic (diameter < 1µm) corresponding to the accumulation mode, micronic (diameter between 1 and 10µm) corresponding to coarse particles and super-micronic or super coarse particles (diameter > 10µm). This treatment in modes is computationally much more efficient compared to a bin-scheme (Schulz et al., 1998). Furthermore, to account for the diversity in chemical composition, hygroscopicity, and mixing state, we distinguish between soluble and insoluble modes. In both sub-micron and micron size, soluble and insoluble aerosols are treated separately. Sea-salt, SO_4, NO_3, and methane sulfonic acid (MSA) are treated as soluble components of the aerosol, dust is treated as insoluble, whereas black carbon (BC) and particulate organic matter (POM) appear both in the soluble and insoluble fractions. The ageing of primary insoluble carbonaceous particles transfers insoluble aerosol number and mass to soluble with a half-life of 1.1 days.

The aerosol scheme is thoroughly explained in Schulz (2007) and Balkanski (2011). Nitrate aerosols were recently added in the INCA model in the framework of ECLAIRE and the results described by Hauglustaine et al. (2014). Characteristic global aerosol properties of the INCA model have been described and compared in all AeroCom publications, as for instant recently in Myhre et al. (2013) and Koffi et al. (2012). We also refer to Szopa et al. (2012) for a simulation of the global aerosol components (excluding nitrates) and tropospheric ozone distributions and their associated radiative forcings between 1850 and 2100 following a recent historical emission dataset (Lamarque et al., 2010) and under the representative concentration pathways (RCP) (Lamarque et al., 2011) for the future with the same version of the model.

Biogenic emissions of VOCs from the continental biosphere and of NO from soils are calculated based on the ORCHIDEE biosphere model as described in Lathière et al. (2006). In the framework of ECLAIRE (see D5.3), the parameterization for VOC emissions has been updated: adding new emitted compounds; re-examining all the Emission Factors (EFs) considering state of the art emission schemes and the most recent field measurements; adding a light dependency for almost all emitted species as already carried out for isoprene; activating the leaf age emission correction factor; activating and adapting a multi-layer radiation scheme, and including a CO_2 inhibition for isoprene emissions. The multi-layer radiation scheme in ORCHIDEE is based on Spitter et al. (1986), with the light profile within the canopy determined by the amount of light at the top of the canopy and by the extinction coefficient of the different radiation components. The light follows an exponential decrease with Leaf Area Index (LAI) when going deeper into the canopy. In the model the LAI is divided in up to 17 levels, with the number of levels depending on the LAI value. For each layer, the percentage of sunlit and shaded leaves together with the diffuse and direct component of the solar radiation are calculated. The inhibition effect of increasing atmospheric CO_2 concentrations on isoprene emissions is now quantified in the model based on two different approaches which can be activated: the first one is based on Possell et al. (2005) and one correction factor, depending only on atmospheric CO_2 concentration, is applied to every Plant Functional Types (PFTs); the second is based on Wilkinson et al. (2009) and the correction factor depends on both the atmospheric and the intercellular CO_2 concentrations and therefore varies amongst PFTs.

4.2 Model set up

In D5.1, hindcast simulations for the period 1960, 1970, 1980, 1990, and 2000, have been performed, using ECMWF meteorology for the years 2005-2006. In Hauglustaine et al. (2014) the same model has been used to extend these simulations to 2030, 2050 and 2100 in the framework of the Representative Concentration Pathway (RCP) anthropogenic emission scenarios. In D5.4; the LMDz-INCA model has been adapted to the new anthropogenic emission inventories prepared by IIASA (Klimont et al., 2013; Amman et al., 2013) in the framework of the ECLAIRE/ECLIPSE/PEGASOS EU projects. These emissions are better suited to the simulation of air quality in the future than the RCP scenarios designed for climate simulations. **In all these simulations, VOC biogenic emissions were fixed to their present-day level and only anthropogenic emissions were varied. In this activity (section 4.4), the future VOC biogenic emissions prepared in D5.3 have been used.**

Key message: An updated version of the LMDz-INCA model has been used to evaluate a range of RCP emission scenarios, as well as new air pollution emission inventories developed in the frame of the ECLAIRE/ECLIPSE/PEGASOS projects.

4.3.1 Present sulfate, nitrate and ammonium aerosols concentrations and deposition

In ECLAIRE, the ammonia cycle and nitrate particle heterogeneous formation have been introduced in the LMDz-INCA global model (Hauglustaine et al., 2014). The model treats ammonia and nitrates interactively with the full tropospheric chemistry and the other types of aerosols. An important feature of this new model is that both fine nitrate particle formation in the accumulation mode from nitric acid and ammonia reaction and coarse nitrate particles forming on existing dust and sea-salt particles are considered. The model developed in this work reproduces distributions of nitrates and related species in agreement with previous pioneering studies. **Figure 1** shows the present-day annual mean surface concentration of sulfates ($SO_4^=$), ammonium (NH_4^+) and total (fine + coarse) nitrates (NO_3^-) aerosols. Maximum sulfate concentrations are calculated over regions of high SO_2 emissions with marked maxima reaching 4-5 µg/m^3 over the Eastern United States, Southern and Eastern Europe and China. The concentration of ammonium (associated both with ammonium sulfate and ammonium nitrate) is localized over continental regions and reaches maxima of 1-2 µg/m^3 over the central and eastern United States, 2-3 µg/m^3 in northern Europe and 4-5 µg/m^3 in northern China. These regions combine both high concentrations of sulfates, nitric acid but also high agricultural emissions of NH_3. The distribution of surface nitrates (fine mode + coarse mode) shows very strong concentrations in regions of high ammonia and nitric acid concentrations. This is in particular the case over northern Europe and China with concentrations reaching 4-5 µg/m^3. **Figure 2** decomposes the total surface nitrate concentration shown in **Figure 1** into its three components: accumulation mode, coarse mode on dust particles and coarse mode on sea-salt particles. The conditions for fine mode nitrate particle formation are met over the continents and maximum concentrations are calculated, as already seen in **Figure 1**, over regions of high agricultural emissions of NH_3 or high HNO_3 concentrations. Coarse nitrate on dust follow the distribution of dust particles in the model. High concentrations reaching more than 0.5 µg/m^3, and locally up to 1-3 µg/m^3, are calculated over the Sahara desert and the Saudi Arabian peninsula and extend to the Mediterranean sea and southern Europe; over the western United States and over China. In contrast, coarse nitrate on sea-salt reaches concentrations of 0.5-1 µg/m^3 in coastal areas where high concentrations of sea-salt and nitric acid are met. These two coarse nitrate components add up for a total of about 0.1-0.2 µg/m^3 over the ocean. Over the continents, fine mode nitrates significantly dominate over source regions. However, in coastal regions or in southern Europe all components mix and coarse nitrates can contribute to 30-40% to the total concentration in these specific areas. The patterns of the calculated distribution of coarse nitrates on dust and sea-salt are in fairly good agreement with previous results.

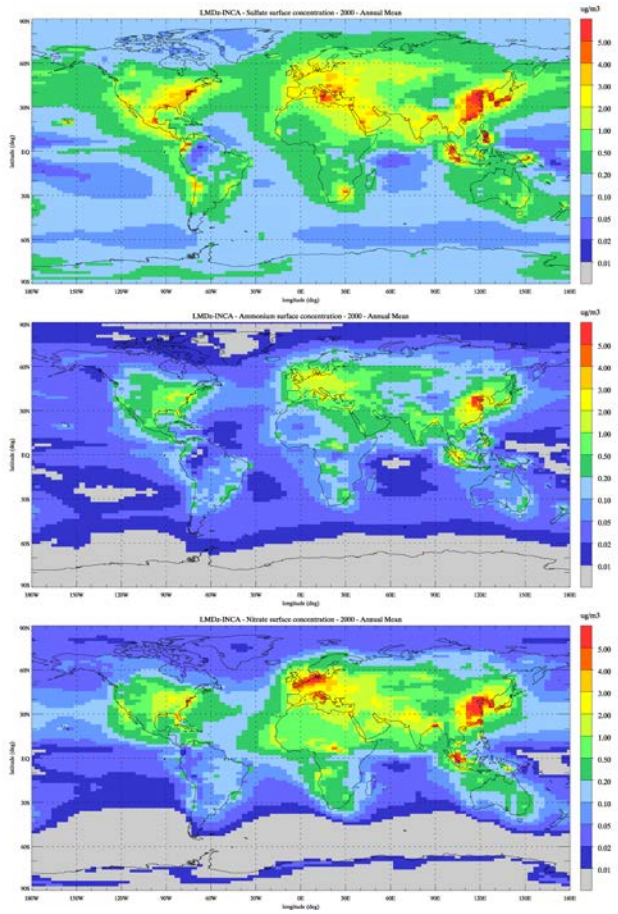

Figure 1: Annual mean surface concentration of (top) sulfate aerosols, (middle) ammonium aerosols, and (bottom) total nitrate aerosols simulated for present-day conditions (µg/m^3) in intervals of 0.01,0.02,0.05,0.1,0.5,1,2,3,4 and 5 µg/m^3

The present-day surface concentrations of sulfates, nitrates, and ammonium have been evaluated by comparison against network measurements from the EBAS database. In Europe and Northern America, the model captures the sulfates measurements with a mean bias of about 20%. As obtained with other models, ammonium and nitrates particles are more difficult to reproduce and higher biases are obtained, reaching, for nitrates, 60% and 100% over Europe and Northern America, respectively. A positive bias in simulated nitrate aerosol concentrations is suspected to be partly linked to negative sampling artefacts in measurements in summer, because evaporation of ammonium nitrate has been frequently reported to create occasionally losses of up to 50%, in particular in warm weather. Further work is needed to better characterize the individual nitrate measurement error, to see where modeled nitrate is consistent with measurements. The model total sulfate, ammonia, and nitrate deposition have also been compared to network measurements. This evaluation shows a reasonable agreement over Europe and Northern America for these three terms, with mean biases of about 20-30% or better. This is not the case in Eastern Asia where systematically underestimated depositions are calculated. This points to the need to further improve the emission inventories in this region and in China in particular. The calculated total aerosol optical depth distribution is generally well reproduced by the model with a mean bias against the AERONET observations of -11%.

Key message: A detailed description of ammonium sulfate-nitrate and coarse-aerosol nitrate formation was included in LMDz-INCA. Good agreement of surface aerosol concentrations and aerosol optical depth was found for Europe and North America. Nitrogen and sulfur deposition were in reasonable agreement in Europe and North America, but systemically underestimated in Eastern Asia.

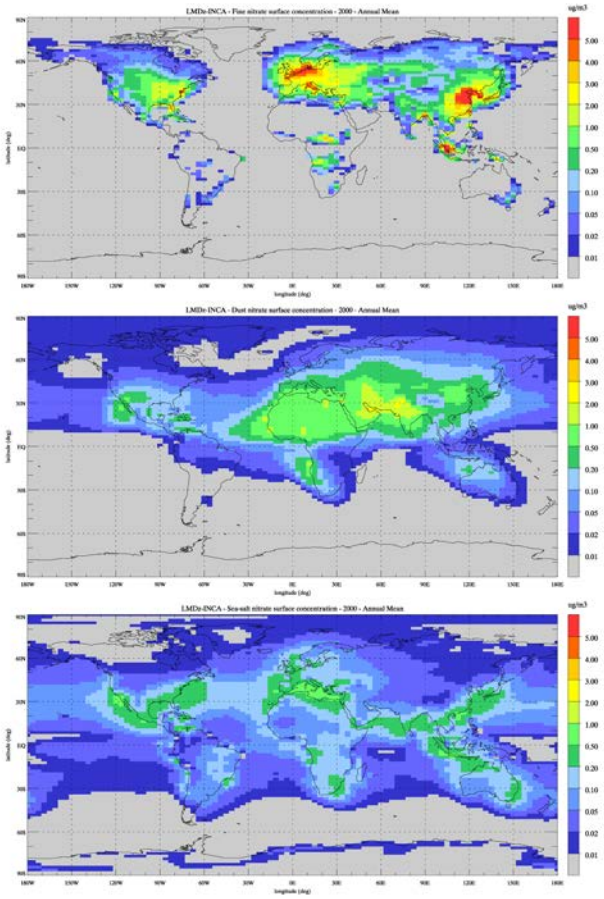

Figure 2. Annual mean surface concentration of (top) fine mode nitrate aerosols, (middle) coarse mode nitrates on dust, and (bottom) coarse mode nitrates on sea-salt simulated for present-day conditions in intervals of 0.01,0.02,0.05,0.1,0.5,1,2,3,4 and 5 μg/m^3 .

4.3.2 Future nitrate aerosols and their direct radiative forcing of climate

The model has been used to investigate the future changes in nitrates and direct radiative forcing of climate based on snapshot simulations for the four Representative Concentration Pathway (RCP) scenarios and for the 2030, 2050 and 2100 time horizons. **Figure 3** presents the evolution in the global burden of nitrate particles and its main precursors for the various scenarios and time-slice experiments. In all scenarios, the burden of fine nitrate particles increases in the atmosphere from a present-day value of 0.05 TgN to 0.13 TgN for RCP8.5 and 0.07 TgN for RCP4.5. As expected, these two extreme values in nitrate are mainly driven by the change in NH_3 emissions and burden. The burden of gaseous NH_3 increases from its present-day value of 0.09 TgN to a maximum value of 0.23 TgN in 2100 in the case of RCP8.5 and to a minimum value of 0.14 TgN for RCP4.5. The formation of coarse nitrate on dust and sea-salt is a result of HNO_3 heterogeneous uptake on these particles. Since no change in climate is considered in these simulations, the burden of dust and sea-salt particles is similar in all simulations. Therefore, the evolution of the coarse nitrate particle burden follows the evolution of the nitric acid in the atmosphere, and decreases from 0.13 TgN to 0.09-0.12 TgN in 2100. Overall, the burden of total nitrate particles increases from 0.181 TgN to 0.183 TgN in 2100 in the case of RCP4.5 and to 0.247 TgN in the case of RCP8.5. The relative contribution of fine particles to this total is however modified and increased from a present-day value 28% to 40% in 2100 for RCP4.5 and to 51% for RCP8.5. Since fine particles contribute the most to the nitrate optical depth and radiative forcing this feature will have consequences on the climate impact of these particles. The future decrease in sulfates leading less ammonium sulfate formation is partially compensated by an increase in ammonia and formation of ammonium nitrate. As a consequence, the NH_4^+ global burden remains fairly constant in time and varies from a present-day value of 0.21 TgN to 0.17-0.24 TgN in 2100.

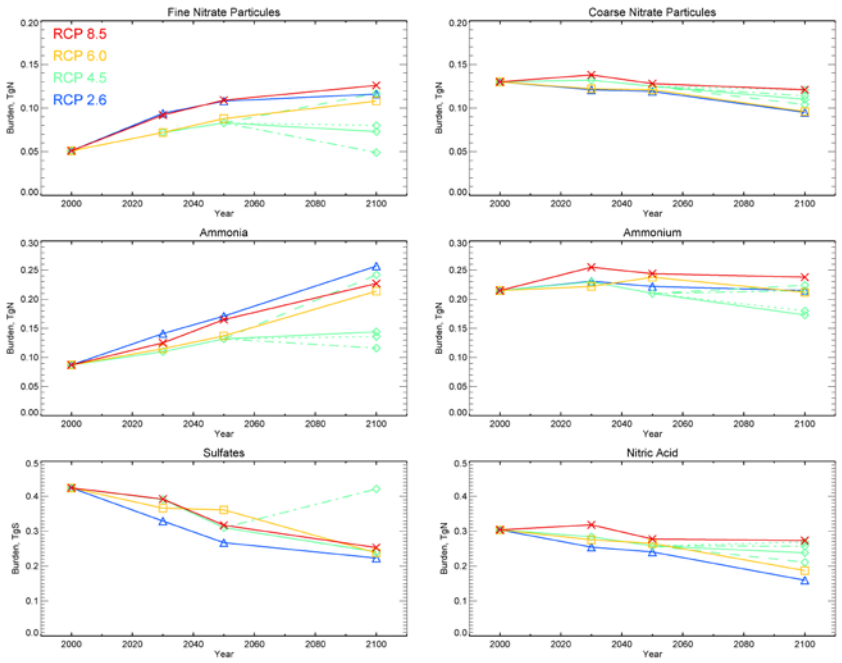

Figure 3. Evolution of the global burden of fine mode nitrates, coarse mode nitrates, ammonia, ammonium, nitric acid (TgN), and sulfates (TgS) for scenario RCP8.5 (red), RCP6.0 (yellow), RCP4.5 (green) and RCP2.6 (blue) between present-day and 2100.

We have also investigated the evolution of total nitrogen deposition (NO_y + NH_x wet and dry deposition) averaged over various regions of the world (see **Figure 4**). In Europe and Northern America, the total N deposition slightly decreases or remains close to its present-day value in the case of scenario RCP8.5. In these regions, the NO_y deposition significantly decreases in the future due to reduced NO_x emissions (from 360 mgN/m^2/yr to 88-150 mgN/m^2/yr in Europe in 2100 and from 265 mgN/m^2/yr to 60-108 mgN/m^2/yr in Northern America). However, this decrease is largely compensated by an increase in NH_x deposition. In Europe for instance, this term increases from 426 mgN/m^2/yr to 672 mgN/m^2/yr in 2100 for RCP8.5. As a consequence, the fraction of N deposited as NH_x increases from about 50% for the present-day to 70-80% in 2100 in these two regions. In Asia and India, the NO_y deposition generally increases in 2030 or 2050 due to higher NO_x emissions in these regions before decreasing at the end of the XXIst century. In addition, the NH_x deposition generally increases during the course of the century to reach maximum values in 2100. As a result, the total N deposition generally reaches a maximum in 2030-2050 and further increases or remains stable until 2100. In Northern Asia (mostly China) for instance, the total deposition increases from 965 mgN/m^2/yr for the present to up to 1443 mgN/m^2/yr in 2050 before decreasing to 880-1251 mgN/m^2/yr in 2100. In India, the deposition increases during the century from a present-day value of 780 mgN/m^2/yr to 1100-1700 mgN/m^2/yr in 2100. As seen in other regions, this increase in total N deposition is also associated with a new balance between NO_y and NH_x deposition. The fraction of N deposited as NH_x increases from about 60% to 80% in these regions. The same tendency is found over oceanic regions and globally. The total N deposited remains fairly stable or slightly decreases in these regions during the XXIst century, but the fraction of N deposited as NH_x increases from 45% to 55-70% over the ocean and from 55% to 70-80% globally. This feature has possible strong consequences for terrestrial or oceanic ecosystems because deposition of nitric acid, which dissociates readily in water causes a significant decline in pH, but deposition of NH_x increases the water alkalinity.

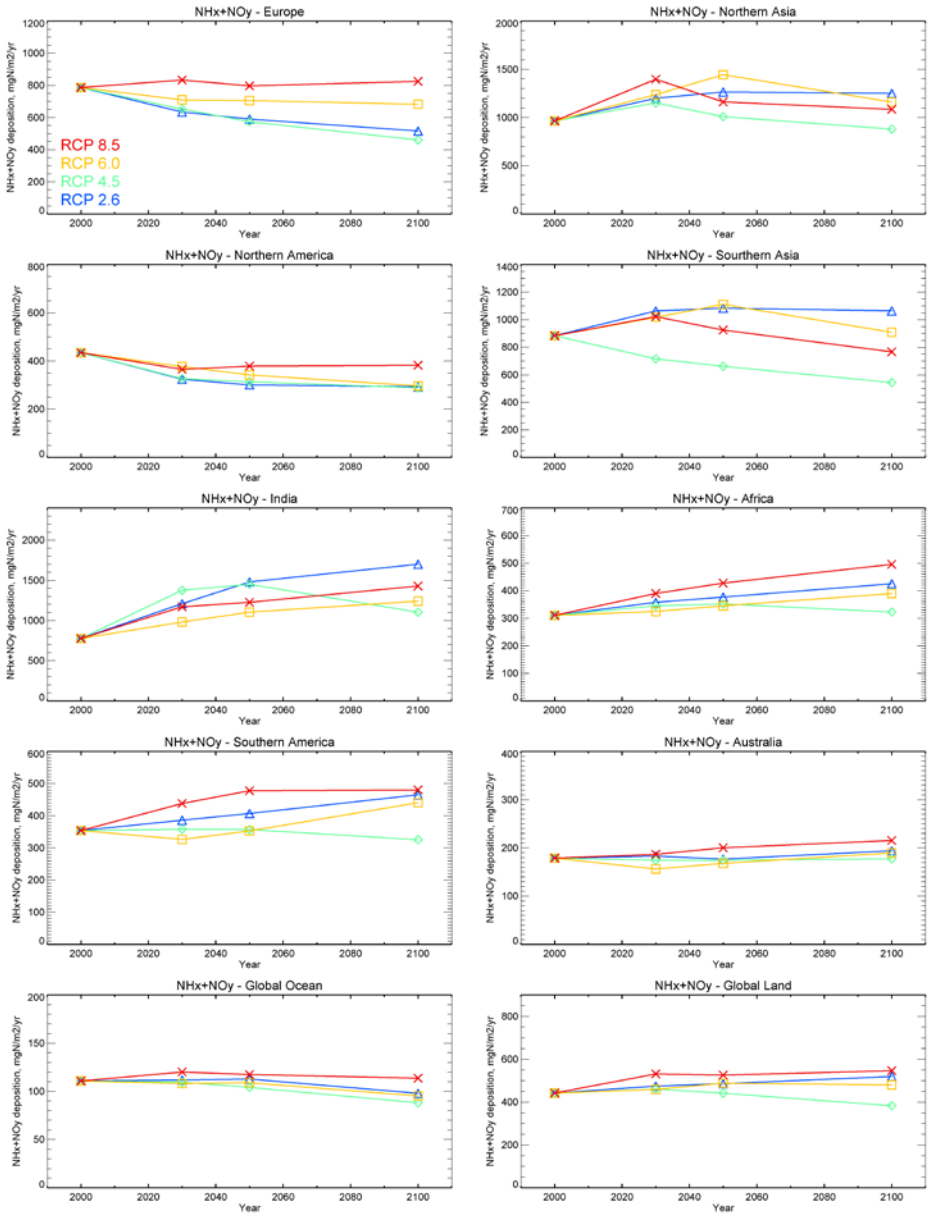

Figure 4. Evolution of total nitrogen deposition (NH_x+NO_y) (mgN/m^2/yr) for scenario RCP8.5 (red), RCP6.0 (yellow), RCP4.5 (green) and RCP2.6 (blue) between the present-day and 2100. The averaged depositions are depicted for Europe, Northern America, Northern Asia, Southern Asia, India, Africa, Souther America, Australia, the global ocean and the globe.

Figure 5 shows the evolution of the radiative forcings associated with the various aerosol components for the different RCP scenarios. As discussed above, the total aerosol forcing decreases from 2000 to 2100 for all scenarios. The negative forcing associated with sulfates decreases from -0.31 W/m^2 in 2000 to a range of -0.03 W/m^2 in RCP 2.6 to -0.08 W/m^2 for RCP8.5. Similarly, the forcing arising from OC decreases from -0.06 W/m^2 in 2000 to -0.03 W/m^2 in 2100 for RCP4.5 and to -0.05 W/m^2 for RCP6.0. In addition, the positive forcing associated with BC decreases from 0.19 W/m^2 in 2000 to 0.04-0.10 W/m^2 in 2100. In contrast, to the other aerosol components, the nitrate negative forcing increases in all scenarios from a present-day value of -0.05 W/m^2 to a value ranging in 2100 from -0.06 W/m^2 for RCP4.5 to -0.11 W/m^2 for RCP8.5. **Figure 6** summarizes the impact of nitrates on the future evolution of the anthropogenic AOD at 550nm and on the direct radiative forcing of aerosols at the top of the atmosphere. The anthropogenic aerosol optical depth generally decreases for all scenarios. Nitrates have an increasing contribution to this AOD and their contribution increases the AOD in 2100 from a factor of 1.8 for RCP6.0 to a factor of 2.8 for RCP2.6. The total aerosol forcing significantly decreases for all scenarios as a consequence of emission reduction for the main aerosols and aerosol precursors. In contrast, we have seen that the negative nitrate forcing increases in the future for all scenarios due to higher emissions of NH_3 from agriculture. Including nitrates in the radiative forcing calculations significantly increases the total direct forcing of aerosols by a factor of 1.3 in 2000, by a factor of 1.7-2.6

in 2030, by 1.9-4.8 in 2050, and by 6.4-8.6 in 2100. These results show that due to increasing NH_3 emissions from agriculture in the future, nitrates have the potential to maintain the aerosol forcing at significantly higher values than expected without including them in the climate simulations and become the main component contributing to this forcing.

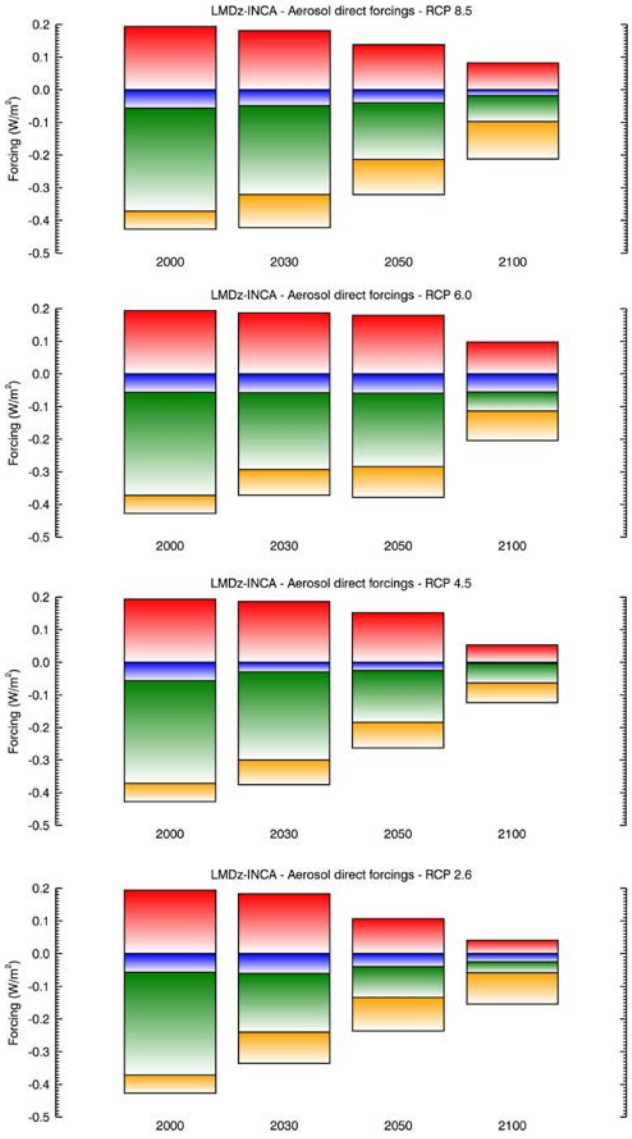

Figure 5. All-sky top of the atmosphere direct radiative forcing (W/m^2) of nitrates (yellow), sulfates (green), organic carbon (blue), and black carbon (red) calculated for the four RCP scenarios and from the present-day to 2100.

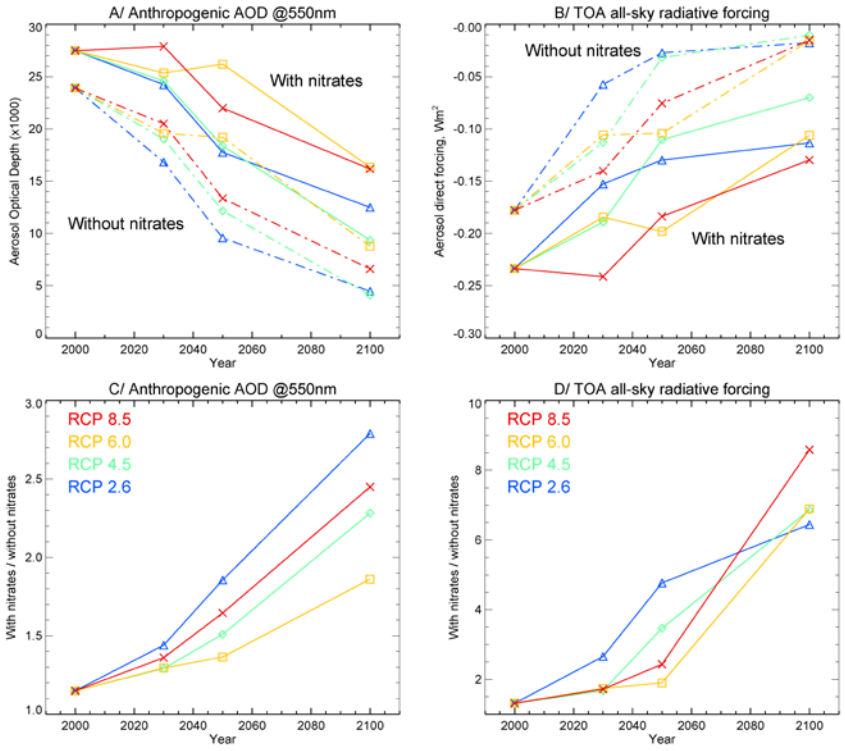

Figure 6. Evolution of A/ the aerosol anthropogenic optical depth at 550nm (X1000) and B/ all-sky top of the atmosphere direct radiative forcing (W/m^2) for the four RCP scenarios and from present-day to 2100; RCP8.5 (red), RCP6.0 (yellow), RCP4.5 (green) and RCP2.6 (blue) Solids lines: nitrates included; dashed lines: nitrates excluded. Corresponding fractional contribution of nitrates to the C/ anthropogenic aerosol optical depth and D/ direct radiative forcing.

Key message: Model calculations suggest under the RCP scenarios SO4 burden is strongly declining, while nitrate and ammonium aerosol burdens are more constant. Agricultural emission of NH3 may therefore maintain higher levels of cooling than assumed in previous studies. The fraction of ammonium in nitrogen deposition is increasing from about 60-80 % in China. These results are driven by increasing agricultural ammonia emissions in the RCP emission scenario, subject to high uncertainty.

4.4 Impact of future VOC biogenic emissions on tropospheric chemistry

As described in D5.3, BVOC emissions have been calculated with the ORCHIDEE vegetation model for present and future (2050) conditions at the global scale. Different simulations have been performed in order to isolate and compare the effects of future change in climate, land-use and CO_2 (inhibition effect on isoprene) on BVOC emission changes. For 2050 global annual emissions are estimated to increase by 25% for isoprene, 27% for monoterpenes and 28% for methanol, compared to the present. When the CO_2 inhibition effect is considered, as described by Wilkinson et al. (2009), a decrease by 9% is calculated for global annual isoprene emissions compared to the present-day scenario, therefore totally counteracting the effect of future change in climate. **Table 1** summarizes the calculated global emissions of key species under the various scenarios considered in this study.

Table 1. Global emissions of key BVOCs calculated with the ORCHIDEE model for present-day conditions and for 2050 conditions. For 2050 conditions different scenarios are considered including climate change and CO_2 fertilization (CC), land-use changes (LU), CO_2 inhibition of isoprene emissions parameterized according to Wilkinson et al. (2009) (IN_W) and CO_2 inhibition of isoprene emissions parameterized according to Possell et al. (2005) (IN_P). (TgC/yr).

	Isoprene	Monoterpenes	Methanol	Acetone
Present-day	393	129	0.36	0.30
2050 CC	503	166	0.46	0.39
2050 CC + LU	490	161	0.45	0.38
2050 CC + LU + IN_W	378	161	0.45	0.38
2050 CC + LU + IN_P	317	161	0.45	0.38

These emissions have been used in the LMDz-INCA model in order to assess the relative importance of future anthropogenic and biogenic emissions on atmospheric chemistry. Simulations are performed for 2010 and 2050 conditions with ECLIPSE5.0 CLE anthropogenic emissions. As an example of these changes in atmospheric composition, **Figure 7** shows the surface ozone calculated in June-July-August for 2010 and 2050 conditions considering these changes in anthropogenic emissions solely and the corresponding change in surface ozone. Under current legislation, and as an effort to improve air quality, ozone decreases by up to 7 ppbv in Northern America and by 4-5 ppb in Europe. In China, SE Asia, and India, ozone increases by up to 7 ppb due to increased anthropogenic emissions in these regions.

Key message: Comparison of the summer ozone distributions between 2050 and 2010 using the ECLIPSE5.0 emission scenario indicates ozone decreases by up to 7 ppbv in Northern America and by 4-5 ppb in Europe. In China, SE Asia, and India, ozone increases by up to 7 ppb due to increased anthropogenic emissions in these regions.

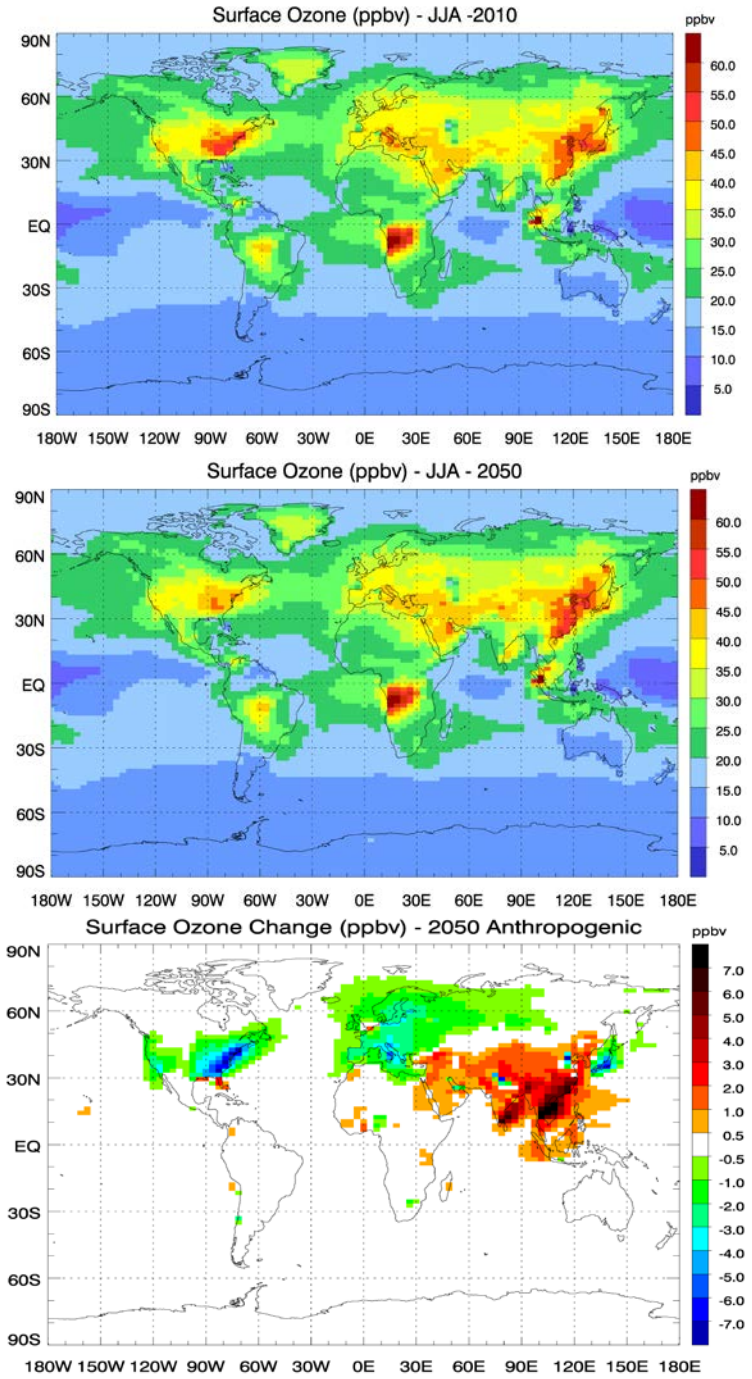

Figure 7: Surface ozone mixing ratio in June-July-August (ppbv) calculated at the surface for the reference present-day scenario (2010) and for the ECLIPSE5.0 CLE future scenario (2050) and difference between the two distributions.

In addition to these future changes in anthropogenic emissions in 2050, future biogenic emissions have been considered and the results compared to the 2050 reference simulation (future anthropogenic but present-day BVOC emissions). **Figure 8** shows the impact of future biogenic emissions on surface ozone in 2050 under various assumptions. When climate change (including CO_2 fertilization) and land-use changes are considered in the calculation of future biogenic emissions, ozone increases by up to 4-4.5 ppbv over China, Northern America and central Europe. In this case the ozone increase partially compensates the ozone decrease due to anthropogenic emissions (**Fig. 7**) over a large part of the northern hemisphere with the exception of China, India, and SE Asia. This increase in ozone is reduced when the CO_2 inhibition is considered for the isoprene emission factors. Two parameterizations have been considered for this CO_2 inhibition. When the Wilkinson et al. (2009) parameterization is used, ozone increases by up to 3 ppbv compared to the 2050 reference simulation with only anthropogenic emissions and when the Possell et al. (2005) parameterization is used the ozone increase in the northern hemisphere is very limited and only reaches 0.5-1 ppb and even decrease in the tropics. These results stress that the CO_2 inhibition can largely compensate, and even dominate depending on the considered parameterization, the increase in BVOC emissions associated with climate change and land-use in the future. More work is however needed to better represent these effects in the vegetation models and hence better understand their role in future atmospheric composition changes.

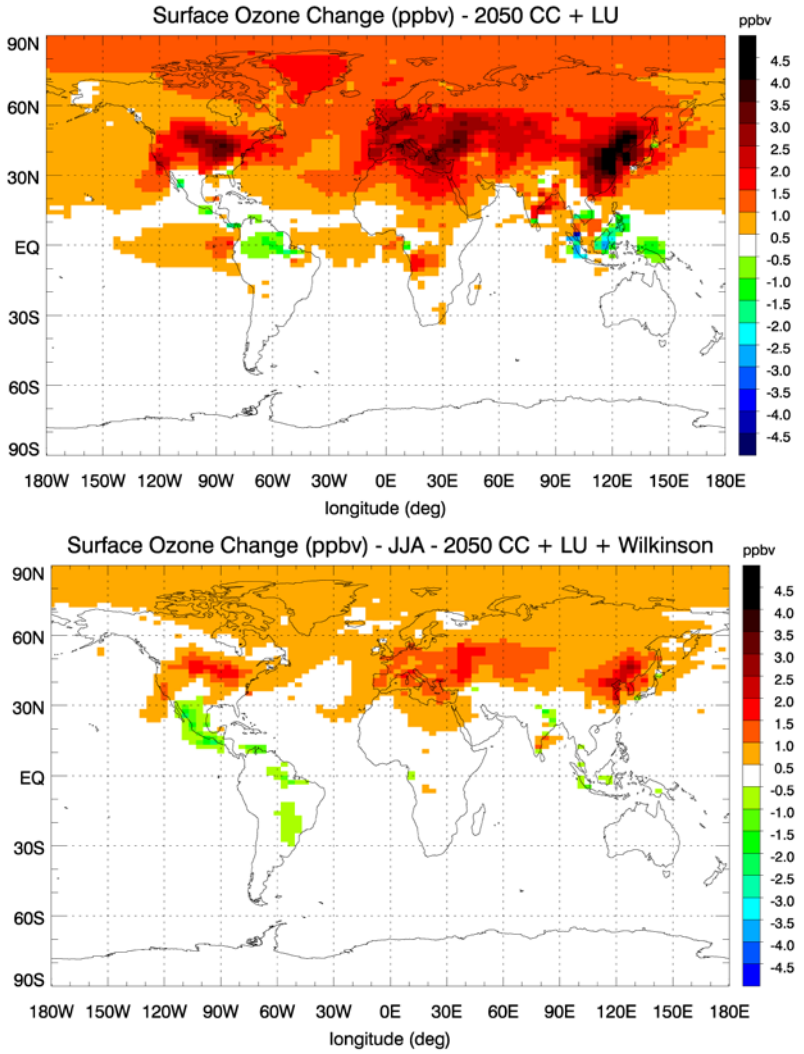

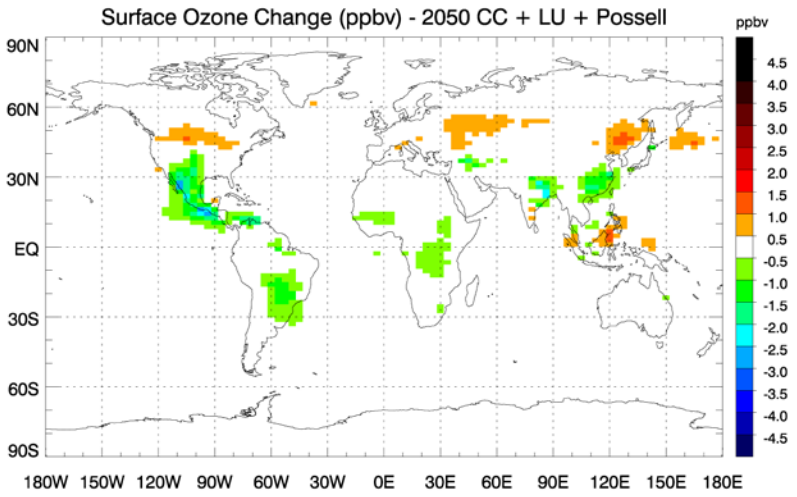

Figure 8. Changes in surface ozone in 2050 relative to the simulation with present-day biogenic emissions due to future biogenic emissions (ppbv). Top panel: climate change including CO_2 fertilization (CC) and land-use (LU) changes considered for future BVOC emissions; middle panel: CC + LU + CO_2 inhibition f for isoprene from Wilkinson (2009); bottom panel: CC + LU + CO_2 with inhibition parameterisation from Possell (2005)

Key message: Comparison of the summer ozone distributions between 2050 and 2010 using the ECLIPSE5.0 emission scenario indicates ozone decreases by up to 7 ppbv in Northern America and by 4-5 ppb in Europe. In China, SE Asia, and India, ozone increases by up to 7 ppb due to increased anthropogenic emissions in these regions. Climate and land use change by 2050 may augment isoprene emission and lead to ozone increases in large portions of the Northern Hemisphere up to 4,5 ppb, potentially off-setting the ozone reductions by anthropogenic emissions in Europe and North America. However, when including the effect of increasing CO2 on reducing the isoprene emissions, the effect on ozone is much less, with two current parameterizations strongly disagreeing.

4. Results from HTAP and TM5-FASST model calculations

5.1 HTAP estimates of concentration changes.

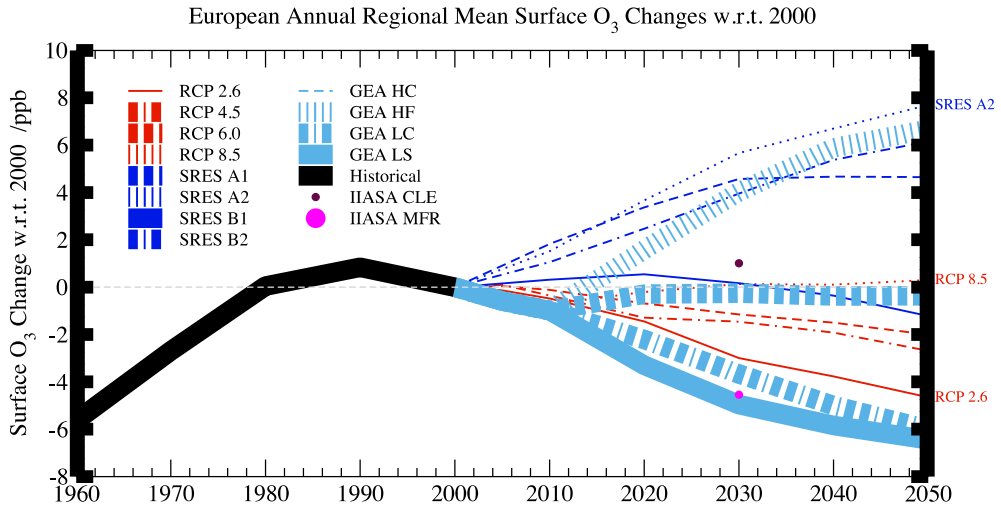

Figure 9: impact of a variety of scenarios on annual average ozone in Europe. HTAP analysis.

Based on model calculations performed for the HTAP(2010) assessment an estimate was made of the ozone changes due to a variety of emission scenarios available around 2012, including RCPs, results from the Global Energy Assessment (Rao et al., 2012) and IIASA GAINS simulations used in a variety of intercomparison studies in the late 2000s (e.g. Dentener et al., 2005).

Using more recent scenarios (ECLIPSEv5) from the IIASA GAINS group an updated estimate is provided to the forthcoming EMEP Assessment report, to be published in 2016. Results suggest that under current legislation assumptions annual average ozone will stabilize at 2010 values, but start increasing again after 2020-2030. Declining contributions from ozone from the US are compensated by increasing ozone from Asia. Growing methane emissions is one of the main contributors to ozone increases in the next decades assuming 'business-as-usual'.

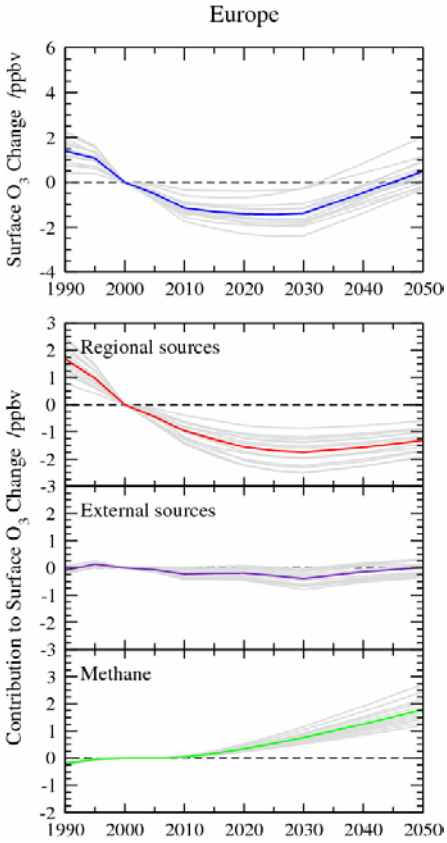

Figure 10. Updated HTAP analysis of future Europe average O3 development according to ECLIPSE5a HTAP scenario.

Analysis with the TM5 FASST model show indeed that the benefits in Europe of implementing maximum feasible emission reductions, will be to a large extent come from other worlds regions, including China, India and the US, whereas the EU contribution would be only 25 %.

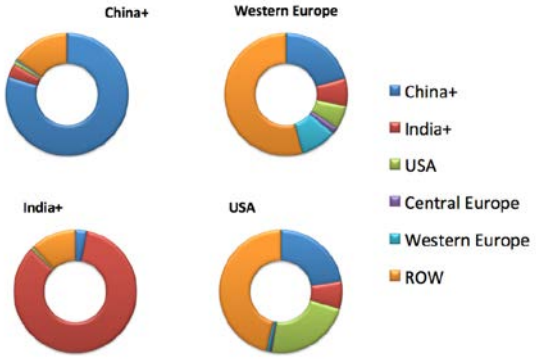

Figure 11, TM5 FASST calculation of the contribution of annual average ozone change due implementation of MFR in 2050, compared to CLE.

Key message: Controlling methane and air pollution emissions in Asia is going to be of critical importance for ozone air quality in Europe.

References

Amann, M., Z. Klimont, and F. Wagner, Regional and global emissions of air pollutants: recent trends and future scenarios, Ann. Rev. Environ. Resourc., 38, 31-55, 2013.

Balkanski, Y., *L'Influence des Aérosols sur le Climat*, Thèse d'Habilitation à Diriger des Recherches, Université de Versailles Saint-Quentin, Saint-Quentin-en-Yvelines, 2011.

Bousquet, P., D. A. Hauglustaine, P. Peylin, C. Carouge, et P. Ciais, Two decades of OH variability as inferred by an inversion of atmospheric transport and chemistry of methyl chloroform, *Atmos. Chem. Phys*., 5, 2635-2656, 2005.

Bousquet, P., C. Yver, I. Pison, Y. S. Li, A. Fortems, D. Hauglustaine, S. Szopa, P. J. Rayner, P. Novelli, R. Langenfelds, P. Steele, M. Ramonet, M. Schmidt, P. Foster, C. Morfopulos, et P. Ciais, A 3D synthesis inversion of the molecular hydrogen cycle: sources and sinks budget implications for the soil uptake, J. Geophys. res., 116, D01302, 2010.

Dentener F., Stevenson, D, Cofala, J., Mechler R., Amann, M., Bergamaschi Peter, Raes Frank, Derwent, R.G. The impact of air pollutant and methane emission controls on tropospheric ozone and radiative forcing: CTM calculations for the period 1990-2030, Atmospheric Chemistry and Physics, 5, 1731-1755, 2005.

Emanuel, K. A., A scheme for representing cumulus convection in large-scale models, J Atmos. Sci., 48, 2313–2335, 1991.

Folberth, G. A., D. A. Hauglustaine, J. Lathière, and F. Brocheton, Interactive chemistry in the Laboratoire de Météorologie Dynamique general circulation model : model description and impact analysis of biogenic hydrocarbons on tropospheric chemistry, Atmos. Chem. Phys., 6, 2273–2319, 2006.

Hauglustaine, D. A., Hourdin, F., Jourdain, L., Filiberti, M. A., Walters, S., Lamarque, J. F., and Holland, E. A.: Interactive chemistry in the Laboratoire de Meteorologie Dynamique general circulation model: Description and background tropospheric chemistry evaluation, J. Geophys. Res., 109, D04314, doi:10.1029/2003JD003957, 2004.

Hauglustaine, D. A., Balkanski, Y., and Schulz, M.: A global model simulation of present and future nitrate aerosols and their direct radiative forcing of climate, Atmos. Chem. Phys., 14, 11031-11063, doi:10.5194/acp-14-11031-2014, 2014.

Hourdin, F. and A. Armengaud, The use of finite-volume methods for atmospheric advection of trace species-1. test of various formulations in a general circulation model, *Month. Weather Rev.,* 127, 822-837, 1999

Hourdin, F. and J. P. Issartel, Sub-surface nuclear tests monitoring through the CTBT xenon network, *Geophys. Res. Lett.*, 27, 2245-2248, 2000.

Hourdin, F., I. Musat, S. Bony, P. Braconnot, F. Codron, J.-L. Dufresne, L. Fairhead, M.-A. Filiberti, P. Friedlingstein, J.-Y. Grandpeix, G. Krinner, P. Levan, Z.-X. Li, and F. Lott, The LMDZ4 general circulation model: climate performance and sensitivity to parametrized physics with emphasis on tropical convection, *Clim. Dyn*., 27, 787–813, 2006.

Klimont, Z., K. Kupiainen, Ch. Heyes, J. Cofala, P. Rafaj, L. Höglund-Isaksson, J. Borken, W. Schöpp, W. Winiwarter, P. Purohit, I. Bertok, and R. Sander, ECLIPSE V4a: Global emission data set developed with the GAINS model for the period 2005 to 2050: Key features and principal data sources, International Institute for Applied Systems Analysis (IIASA), Schlossplatz 1, 2361 Laxenburg, Austria, 2013.

Koffi, B., M. Schulz, F.-M. Breon, J. Griesfeller, D. Winker, Y. Balkanski, S. Bauer, T. Berntsen, M. Chin, W. D. Collins, F. Dentener, T. Diehl, R. Easter, S. Ghan, P. Ginoux, S. Gong, L. W. Horowitz, T. Iversen, A. Kirkevag, D. Koch, M. Krol, G. Myhre, P. Stier, and T. Takemura, Application of the CALIOP layer product to evaluate the vertical distribution of aerosols estimated by global models: AeroCom phase I results, *J. Geophys. Res*., 117, D10201, doi:10.1029/2011JD016858, 2012.

Krinner, G., N. Viovy, N. de Noblet-Ducoudre, J. Ogee, J. Polcher, P. Friedlingstein, P. Ciais, S. Sitch, and I. C. Prentice, A dynamic global vegetation model for studies of the coupled atmosphere-biosphere system, *Global Biogeochem. Cycles*, 19, GB1015, doi: 10.1029/2003GB002199, 2005.

Lamarque J.-F., T. C. Bond, V. Eyring, C. Granier, A. Heil, Z. Klimont, D. Lee, C. Liousse, A. Mieville, B. Owen, M. G. Schultz, D. Shindell, S. J. Smith, E. Stehfest, J. Van Aardenne, O. R. Cooper, M. Kainuma, N. Mahowald, J. R. McConnell, V. Naik, K. Riahi, and D. P. van Vuuren, Historical (1850–2000) gridded anthropogenic and biomass burning emissions of reactive gases and aerosols: methodology and application, *Atmos. Chem. Phys.,* 10, 7017-7039, 2010.

Lamarque, J.-F., G. P. Kyle, M. Meinshausen, K. Riahi, S. J. Smith, D. P. van Vuuren, A. J. Conley, and F. Vitt, Global and regional evolution of short-lived radiatively-active gases and aerosols in the Representative Concentration Pathways, *Climatic Change*, 109:191–212 DOI 10.1007/s10584-011-0155-0, 2011.

Lathière, J., Hauglustaine, D. A., Friend, A., De Noblet-Ducoudré, N., Viovy, N., and Folberth, G.: Impact of climate variability and land use changes on global biogenic volatile organic compound emissions, Atmos. Chem. Phys., 6, 2199–2146, 2006.

Myhre, G., and 40 co-authors, Radiative forcing of the direct aerosol effect from AEROCOM Phase II simulations, *Atmos. Chem. Phys.,* 13, 1853-1877, 2013.

Pison, I., P. Bousquet, F. Chevallier, S. Szopa, and D. Hauglustaine**,** Multi-species inversion of CH4, CO and H2 emissions from surface measurements, *Atmos. Chem. Phys.*, 9, 5281-5297, 2009.

Possell M, Hewitt CN, Beerling DJ (2005) The effects of glacial atmospheric CO2 concentrations and climate on isoprene emissions by vascular plants. Global Change Biology, 11, 60–69.

Rao, S. Vadim Chirkov**, F. Dentener, Rita** Van Dingenen, Shonali Pachauri, Pallav Purohit,Markus Amann, Chris Heyes, Patrick Kinney, Zbigniew Klimont, Keywan Riahi, Wolfgang Schoepp. Environmental Modeling and Methods for Estimation of the Global Health Impacts of Air Pollution, Environ Model Assess, DOI 10.1007/s10666-012-9317, 2012.

Rivier, L., P. Ciais, D. A. Hauglustaine, P. Bakwin, P. Bousquet, P. Peylin, et A. Klonecki, Evaluation of SF6, C2Cl4, and CO to approximate fossil fuel CO2 in the Northern Hemisphere using a chemistry transport model, J. Geophys. Res., 111, D16311, 2006.

Schulz, M., *Constraining Model Estimates of the Aerosol Radiative Forcing***,** Thèse d'Habilitation à Diriger des Recherches, Université Pierre et Marie Curie, Paris VI, 2007.

Schulz, M., Y. Balkanski, F. Dulac, and W. Guelle, Role of aerosol size distribution and source location in a three-dimensional simulation of a Saharan dust episode tested against satellite-derived optical thickness, *J. Geophys. Res*., 103, 10,579–10,592, 1998.

Spitters, C.J.T., Toussaint, H.A.J.M. and Goudriaan, J., 1986. Separating the diffuse and direct component of global radiation and its implications for modeling canopy photosynthesis. Part I. Components of incoming radiation. Agric. For. Meteorol., 38: 217-229.

Szopa, S, Y. Balkanski, M. Schulz, S. Bekki, D. Cugnet, A. Fortems-Cheiney, S. Turquety, A. Cozic, C. Deandreis, D. Hauglustaine, A. Idelkadi, J. Lathiere, M. Marchand, N. Yan, and J.-L. Dufresne, Aerosol and ozone changes as forcing for climate evolution between 1850 and 2100, *Clim. Dyn.*, 40, 2223–2250, DOI 10.1007/s00382-012-1408-y, 2012.

Van Leer, B., Towards the ultimate conservative difference scheme. Part IV: a new approach to numerical convection, *J. Comput. Phys*., 23, 276-299, 1977.

Wilkinson, M. J., Monson, R. K., Trahan, N., Lee, S., Brown, E., Jackson, R. B., Polley, H. W.,Fay P. A., Fall, R. (2009). Leaf isoprene emission rate as a function of atmospheric CO2 concentration. Global Change Biology, 15(5), 1189-1200.

5. Milestones achieved

Model simulations and

6. Deviations and reasons

Model analysis was delayed due to computing resource problems. HTAP analysis was late due late delivery of scenarios.

7. Publications

Hauglustaine, D. A., Balkanski, Y., and Schulz, M.: A global model simulation of present and future nitrate aerosols and their direct radiative forcing of climate, *Atmos. Chem. Phys*., 14, 11031-11063, doi:10.5194/acp-14-11031-2014, 2014.

Myhre, G., and 40 co-authors, Radiative forcing of the direct aerosol effect from AEROCOM Phase II simulations, *Atmos. Chem. Phys.,* 13, 1853-1877, 2013.

Likhvar, V., M. Pascal, K. Markakis, A. Colette, D. Hauglustaine, M. Valary, Z. Klimont, S. Medina, P. Kinney, A Multi-Scale Health Impact Assessment of Air Pollution Over the 21st Century, Accepted for publication *Science of the Total Environment*, 2015.

8. Meetings

Participation in ECLAIRE plenary meeting, TF HTAP, EMEP Steering Body meetings.

9. List of Documents/Annexes:

None.